HAL

open science

Subtropical dipole modes simulated in a coupled general circulation model

Yushi Morioka, Tomoki Tozuka, Sébastien Masson, Pascal Terray, Jing-Jia Luo, Toshio Yamagata

▶ **To cite this version:**

HAL Id: hal-00758345

https://hal.science/hal-00758345

Submitted on 24 Oct 2021

Subtropical Dipole Modes Simulated in a Coupled General Circulation Model

Yushi Morioka and Tomoki Tozuka

Department of Earth and Planetary Science, Graduate School of Science, The University of Tokyo, Tokyo, Japan

Sebastien Masson and Pascal Terray

LOCEAN/IPSL, Université Pierre et Marie Curie, Paris, France

Jing-Jia Luo

Research Institute for Global Change, JAMSTEC, Yokohama, Japan

Toshio Yamagata

Department of Earth and Planetary Science, Graduate School of Science, The University of Tokyo, Tokyo, Japan

ABSTRACT

The growth and decay mechanisms of subtropical dipole modes in the southern Indian and South Atlantic Oceans and their impacts on southern African rainfall are investigated using results from a coupled general circulation model originally developed for predicting tropical climate variations. The second (most) dominant mode of interannual sea surface temperature (SST) variations in the southern Indian (South Atlantic) Ocean represents a northeast–southwest oriented dipole, now called subtropical dipole mode. The positive (negative) SST interannual anomaly pole starts to grow in austral spring and reaches its peak in February. In austral late spring, the suppressed (enhanced) latent heat flux loss associated with the variations in the subtropical high causes a thinner (thicker) than normal mixed layer thickness that, in turn, enhances (reduces) the warming of the mixed layer by the climatological shortwave radiation. The positive (negative) pole gradually decays in austral fall because the mixed layer cooling by the entrainment is enhanced (reduced), mostly owing to the larger (smaller) temperature difference between the mixed layer and the entrained water. The increased (decreased) latent heat loss due to the warmer (colder) SST also contributes to the decay of the positive (negative) pole. Although further verification using longer observational data is required, the present coupled model suggests that the South Atlantic subtropical dipole may play a more important role in rainfall variations over the southern African region than the Indian Ocean subtropical dipole.

1. Introduction

Southern Africa (Africa south of the equator in general) experiences most of the annual rainfall in austral summer and its interannual variation has a significant socioeconomic impact on the regional society. A number of studies have been devoted to investigate its possible link with the El Niño–Southern Oscillation (ENSO) in the Pacific (Ropelewski and Halpert 1987; Lindesay 1988;

Mason 1995; Reason et al. 2000; Richard et al. 2000). However, they are not sufficient to explain all of the interannual variability. Recently, much attention has been paid to studying impacts from regional sea surface temperature (SST) anomalies in the southern Indian and South Atlantic Oceans (Walker 1990; Mason 1995; Reason 1998; Reason and Mulenga 1999; Behera and Yamagata 2001; Reason 2001; Fauchereau et al. 2009). This is clearly seen in Fig. 1a, showing the correlation between the SST anomalies and the southern African rainfall index (SARI) (Richard et al. 2000), defined as area-averaged land rainfall anomalies south of 10°S during 1960–2008. The SST anomalies in the southwestern (northeastern) region of the southern Indian and South Atlantic Oceans are positively (negatively)

Corresponding author address: Toshio Yamagata, Department of Earth and Planetary Science, Graduate School of Science, The University of Tokyo, 7-3-1, Hongo, Bunkyo-ku, Tokyo 113-0033, Japan.
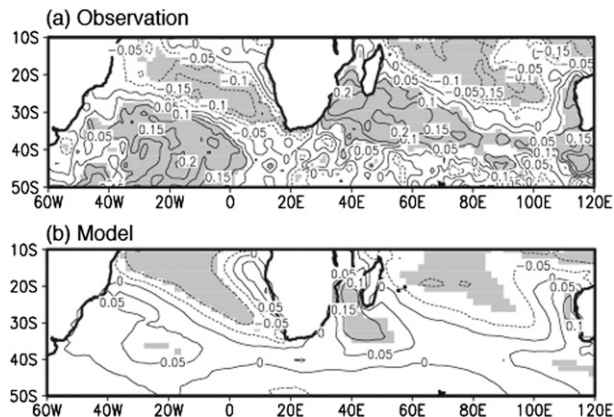E-mail: yamagata@eps.s.u-tokyo.ac.jp

FIG. 1. Correlation between the (a) observed and (b) simulated SARI and SST anomalies: correlations exceeding 90% confidence level by a two-tailed t test are shaded.

correlated with the SARI, representing a clear dipole structure. This dipole pattern is also obtained even when rainfall indices are defined using the rainfall anomaly south of 5° or 15°S.

The existence of this dipole pattern was first identified in the southern Indian Ocean by Behera et al. (2000). Using observations and a reanalysis dataset, Behera and Yamagata (2001) revealed that the SST anomalies associated with the named Indian Ocean subtropical dipole (IOSD) reach their peak in February owing to the latent heat flux anomalies associated with the variations in the Mascarene high. This important role of the latent heat flux anomalies was also supported by calculating a mixed layer heat balance with a constant thickness (Suzuki et al. 2004; Hermes and Reason 2005).

Another dipole of SST anomalies in the South Atlantic is known as the South Atlantic subtropical dipole (SASD). Using a singular value decomposition (SVD) analysis, Venegas et al. (1997) first showed the existence of dipole SST anomalies in the South Atlantic and its link with variations in the sea level pressure (SLP). Later, Fauchereau et al. (2003) suggested that the SST anomalies associated with the SASD are mostly due to the latent heat flux anomalies linked with the southward migration and strengthening of the St. Helena high. The importance of the latent heat flux anomalies was also discussed using ocean assimilation data (Sterl and Hazeleger 2003) or outputs from an ocean general circulation model (OGCM) (Colberg and Reason 2007).

However, all of these studies on the IOSD and SASD were based on a discussion of the heat balance in a box with a constant mixed layer thickness. Since the mixed layer depth undergoes significant seasonal and interannual variations in the subtropics, those studies may have serious defects. Indeed, Morioka et al. (2010, 2011)

have recently revealed the significance of interannual variations in the mixed layer thickness on the growth of SST anomalies associated with the IOSD and SASD, respectively. They indicated that warming of the mixed layer by climatological shortwave radiation is enhanced (reduced) because of the thinner (thicker) than normal mixed layer over the positive (negative) SST anomaly pole. However, these results were based on the outputs from an OGCM in which the surface heat fluxes were calculated by the bulk formula using the atmospheric reanalysis data and the simulated SST. As a result, some effects of the SST anomaly on surface heat fluxes are neglected. For instance, the positive SST anomaly pole in reality acts to enhance the moisture (temperature) of air near the ocean surface and reduce the latent (sensible) heat loss from the ocean. To reveal the air–sea interaction processes involving the IOSD and SASD in more detail, it is necessary to use a coupled general circulation model (CGCM).

Furthermore, impacts of the subtropical dipole modes on the southern African rainfall are still unclear. Using outputs of an atmospheric general circulation model (AGCM), Reason (2001, 2002) showed that the positive SST anomaly of positive IOSDs enhances the rainfall in austral summer via anomalous moisture convergence associated with the low SLP anomalies generated over the positive SST anomaly pole. To understand variations of the southern African rainfall related to air–sea interaction involving the IOSD, a one-tier approach using a CGCM may also be necessary. Using observational and reanalysis data, Vigaud et al. (2009) suggested a potential impact of the dipole SST anomalies in the South Atlantic on the rainfall anomalies during austral summer. Since the 1979–2000 data period used in their study is too short, only one positive SASD event and three negative SASD events are selected in their composite analysis, which is not sufficient to examine the link between the SASD and rainfall variations.

Therefore, the present study investigates the growth and decay of subtropical dipole modes using outputs from a 500-yr integration of a CGCM and examines their impact on the southern African rainfall. This paper is organized as follows. A brief description of the data and the CGCM is given in the next section. The seasonal variation of observed and simulated SST and mixed layer depth in the southern Indian Ocean is discussed in section 3. In section 4, we compare the observed and simulated IOSD and SASD. The mixed layer heat balance over the SST anomaly poles for the positive IOSD is investigated in section 5. In section 6, the impacts of the positive IOSD and SASD on the southern African rainfall in austral summer are examined. The final section summarizes the main results and discusses the difference in the position

of SST anomaly poles associated with the subtropical dipole modes between the observations and model.

2. Model and data

We use monthly mean outputs from a CGCM developed at the Frontier Research Center for Global Change (FRCGC) called the Scale Interaction Experiment-FRCGC (SINTEX-F) model (Luo et al. 2003). The SINTEX-F model has been developed from the original European SINTEX model under the Japan–European Union collaboration (Gualdi et al. 2003; Guilyardi et al. 2003) and a more detailed model description is provided by Luo et al. (2005). The oceanic component is based on the reference version 8.2 of Océan Parallélisé (OPA) (Madec et al. 1998). Its horizontal resolution is $0.5°$–$2°$, with the meridional resolution increasing up to $0.5°$ near the equator, and it has 31 vertical levels with 19 levels in the upper 500 m. The vertical eddy viscosity and diffusivity are calculated from a 1.5-order turbulent closure scheme (Blanke and Delecluse 1993), and the Gent and McWilliams (1990) scheme is included for the isopycnal mixing. Sea ice cover in the model is given by observed monthly climatology.

The atmospheric component of the model is the latest version of the ECHAM4 (Roeckner et al. 1996). Our configuration is based on a T106 Gaussian grid and 19 levels in the hybrid sigma-pressure vertical. Surface turbulent heat flux is calculated by a bulk aerodynamic formula in which the drag coefficients for momentum and heat depend on the moist bulk Richardson number and roughness length (Louis 1979). For cumulus convection, the bulk mass flux formula of Tiedtke (1989) is used.

The atmospheric and oceanic fields are coupled every 2 h by the Ocean Atmosphere Sea Ice Soil (OASIS) 2.4 coupler (Valcke et al. 2000). The surface current momentum is directly passed to the atmosphere through a vertical viscosity term in its momentum equation. The initial condition of the ocean is from the Levitus annual mean climatologies with zero velocities. For the atmosphere, a 1-yr run forced with the observed monthly climatological SST is used. To obtain a sufficient number of SASD and IOSD events for a discussion of their relative impact on the southern African rainfall, the coupled model is integrated for 520 years. Considering the near-surface oceanic adjustment time, we analyze outputs from the last 500 years.

For comparison, we use the monthly mean observed SST data from the Hadley Centre sea ice and sea surface temperature (HADISST) (Rayner et al. 2003), gridded data with $1° \times 1°$ resolution, and we analyze the period during 1960–2008 because of few observations in the southern Indian and South Atlantic Oceans before the

1960s. To derive the mixed layer depth, we use the monthly climatology of ocean temperature available from the *World Ocean Atlas 2009* (*WOA09*) (Locarnini et al. 2010; http://www.nodc.noaa.gov), which has 24 levels in the vertical with $1° \times 1°$ horizontal resolution. We also use the horizontal wind at 850 hPa from the National Centers for Environmental Prediction–National Center for Atmospheric Research (NCEP–NCAR) reanalysis dataset (Kalnay et al. 1996). It has a $2.5° \times 2.5°$ horizontal resolution and covers the same period. Regarding precipitation, we use the gridded monthly rainfall data, provided by the University of Delaware (Legates and Willmott 1990), from 1960 to 2008 with a horizontal resolution of $0.5°$ in both longitude and latitude. For all of these data the interannual anomalies are calculated by subtracting the monthly mean climatology after removing a linear trend using a least squares fit.

The correlation between the simulated SARI and SST interannual anomalies is shown in Fig. 1b. The model reproduces northeast–southwest oriented dipoles in the South Atlantic and southern Indian Oceans rather well. The simulated IOSD and SASD are compared with the observed ones in Fig. 2. The IOSD in the observation is captured by the second EOF mode (Fig. 2a), whereas in the model it is captured by the first EOF mode (Fig. 2b). The pattern correlation between them is 0.88 and is remarkably high. This is superior compared with other CGCMs as shown by Kataoka et al. (2012). Therefore, the model has high skill in simulating the SST pattern associated with the IOSD. On the other hand, both observed and simulated SASD are detected as the first EOF mode (Figs. 2c,d). Although the northeast–southwest orientation of the poles is well simulated, the position of the positive pole in the model is shifted toward higher latitudes by $10°$; the pattern correlation is 0.76. Also, the percentage of the explained variance in the model for the IOSD (SASD) is 20.2% (19.2%) and is in good agreement with 21.0% (20.4%) in the observation. The second EOF mode with a monopole pattern simulated in the southern Indian Ocean and the South Atlantic explains 14.6% and 14.0% of the total variance, respectively, and is sufficiently separated from the first mode (North et al. 1982).

Furthermore, we have defined positive (negative) event years as years when the normalized principal component during austral summer (in Fig. 2) exceeds one (minus one) standard deviation. This leads to 9 (7) positive IOSD (SASD) events during 49 years in the observation and 74 (76) positive IOSD (SASD) events during 500 years in the model. The frequency of occurrence for the observed positive IOSDs (SASDs), 18.8% (14.6%), is well reproduced in the model, 14.8% (15.2%). Thus, the use of this model for analyses of the IOSD and SASD may be validated.
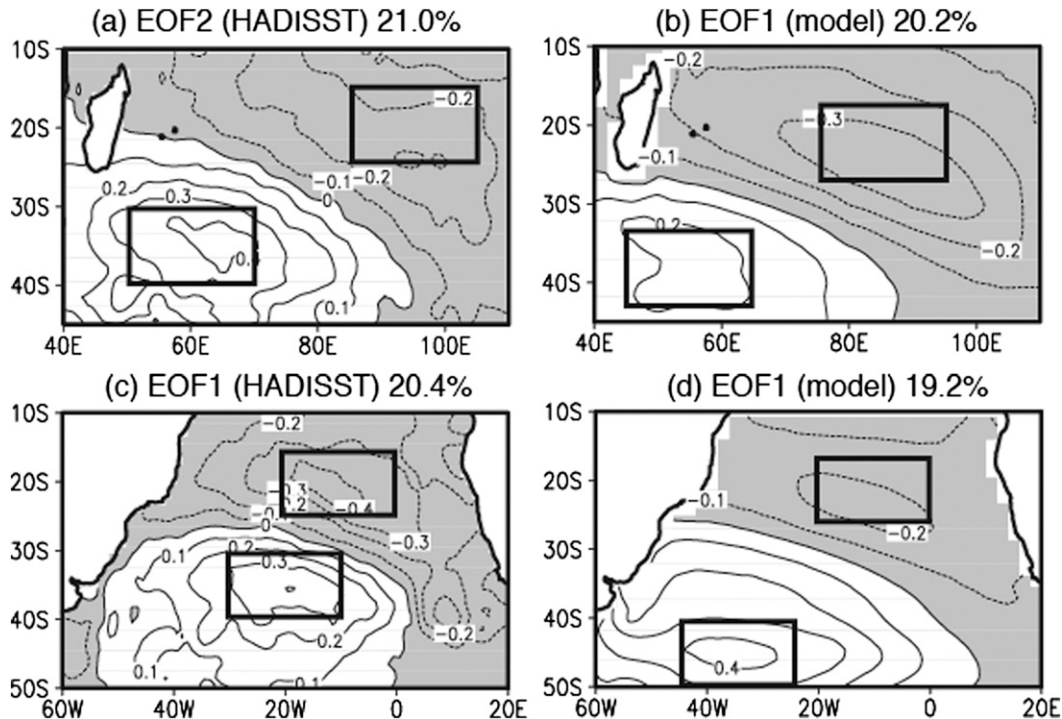
FIG. 2. Spatial patterns of the (a) second EOF mode of SST anomalies from HADISST and (b) first EOF mode of SST anomalies from SINTEX-F model in the southern Indian Ocean, and the first EOF mode of SST anomalies from (c) HADISST and (d) the model in the South Atlantic (°C). Negative values are shaded, and percentage of the explained variance is shown. The boxes over the positive and negative poles in the upper left (right) panel are defined as 30°–40°S, 50°–70°E (33° and 43°S, 45° and 65°E) and 15°–25°S, 85°–105°E (17° and 27°S, 75° and 95°E). The boxes over the positive and negative poles in the lower left (right) panel are defined as 30°–40°S, 10°–30°W (40° and 50°S, 23° and 43°W) and 15°–25°S, 0°–20°W (16° and 26°S, 0° and 20°W).

3. Validation of simulated seasonal variability in the subtropical region

In this section, we explore the seasonal variation of the SST and mixed layer depth in the subtropical region to help understand its interannual variation. Since results obtained in the South Atlantic are almost similar, we discuss only the seasonal variation in the southern Indian Ocean. Both observed and simulated SST averaged over the southwestern pole (33°–43°S, 45°–65°E), defined in Fig. 2b, show a clear annual cycle with their maximum in February (Fig. 3a), whereas those over the northeastern pole (17°–27°S, 75°–95°E) reach their peak in March (Fig. 3b). To investigate this seasonal SST variation, we use the tendency of the mixed layer temperature T_m averaged over the box of each pole:

$$\frac{\partial T_m}{\partial t} = \frac{Q_{\text{net}} - q_d}{\rho c_p H} - \mathbf{u}_m \cdot \nabla T_m - \frac{\Delta T}{H} w_e + \text{res} \qquad (1)$$

(Qiu and Kelly 1993; Moisan and Niiler 1998). The first term on the right-hand side indicates the contribution from the surface heat flux, where Q_{net} is the net surface heat flux, q_d is the downward solar insolation penetrating through the mixed layer bottom (Paulson and Simpson 1977), ρ ($=1027$ kg m^{-3}) is the density of the seawater, c_p ($=4187$ J kg^{-1} K^{-1}) is the specific heat of the seawater, and H is the mixed layer depth, defined as the depth at which temperature is 0.5°C lower than the SST. Here q_d is negligible compared to Q_{net} because only less than 5% of the shortwave radiation can penetrate the mixed layer depth, even when the mixed layer is thinnest in austral summer. The second term indicates the horizontal advection, where $\mathbf{u}_m$ denotes the horizontal velocity averaged in the mixed layer. The third term is the entrainment term, where ΔT ($\equiv T_m - T_{-H-20\text{m}}$) represents the temperature difference between the mixed layer and the entrained water; we use the water temperature at 20 m below the mixed layer base as the temperature of entrained water, as in Yasuda et al. (2000). Also, w_e ($\equiv \partial H/\partial t + \nabla \cdot \mathbf{u}_m H$) is the entrainment velocity and is assumed to vanish when it becomes negative (Kraus and Turner 1967; Qiu and Kelly 1993). The residual term, res, consists of diffusion, detrainment, and other
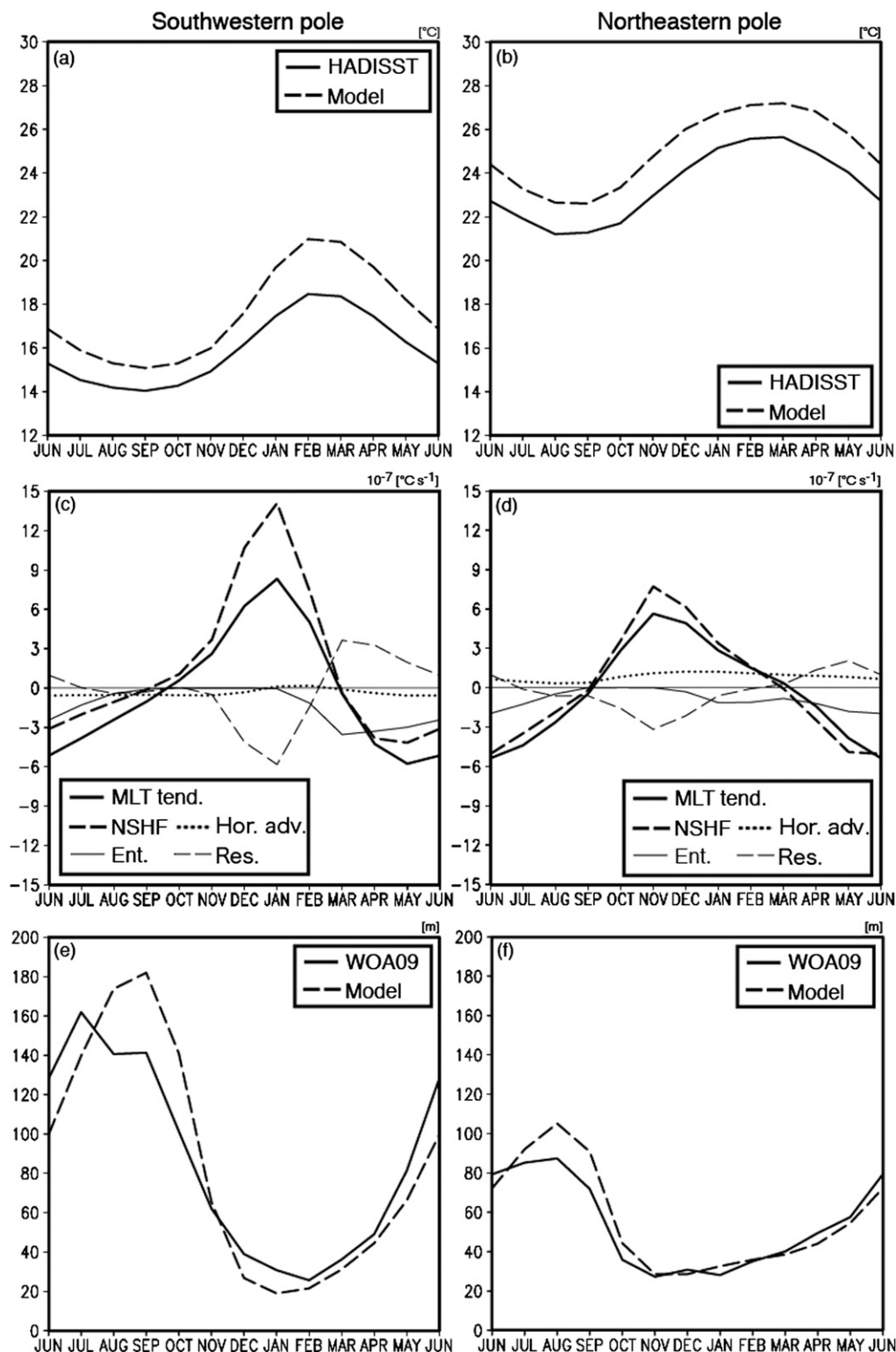
FIG. 3. Seasonal cycle of (a),(b) SST (°C), (c),(d) each term in Eq. (1) (10^{-7} °C s^{-1}), and (e),(f) mixed layer depth (m) at the southwestern and northeastern poles of the IOSD defined in Fig. 2b. In (a),(b) the SSTs from HADISST (solid line) and SINTEX-F model (dashed line) are shown. In (c),(d) the mixed layer temperature tendency (MLT tend., thick solid line), net surface heat flux (NSHF, thick dashed line), horizontal advection (Hor. adv., thick dotted line), entrainment (Ent., thin solid line) and residual (Res., thin dashed line) terms are shown. In (e),(f), the mixed layer depths derived from *WOA09* (solid line) and the model (dashed line) are shown.
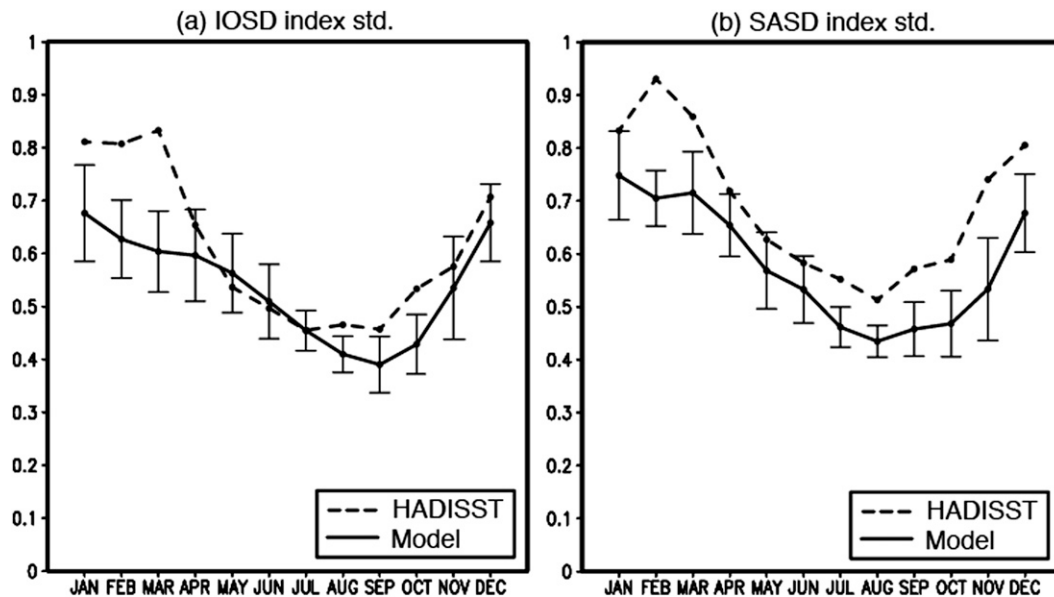
FIG. 4. Monthly standard deviation of (a) IOSD and (b) SASD indices (°C) from HADISST (dashed line) and SINTEX-F model (solid line). The error bar indicates one standard deviation calculated using 10 different 49-yr periods.

neglected oceanic processes such as high frequency variability.

The monthly climatology of each term in Eq. (1) over the southwestern (northeastern) pole is shown in Fig. 3c (Fig. 3d). The warming of the mixed layer over the southwestern (northeastern) pole from November to February (from October to March) is mostly due to the contribution from the net surface heat flux. Among its four components, the contribution from shortwave radiation is dominant (figure not shown). The shallow mixed layer also contributes to enhanced warming of the mixed layer by shortwave radiation (Figs. 3e,f). The contribution from shortwave radiation over the southwestern (northeastern) pole decreases from March to September (from April to September), explaining most of the mixed layer cooling. Also, cooling of the mixed layer by entrainment occurs when the mixed layer deepens (Figs. 3e,f). The mixed layer depth in the model at the southwestern (northeastern) pole becomes deepest in September (August) and its seasonal variation is well simulated.

4. Validation of simulated interannual variability in the subtropical region: Subtropical dipole modes

To identify the key feature of the observed and simulated SST anomalies associated with the IOSD and SASD, we introduce IOSD and SASD indices, defined by the difference in the SST anomalies between the boxes over the southwestern and northeastern poles (Figs. 2a–d). Each of the observed and simulated IOSD (SASD)

indices shows a high correlation, above 0.9, with the principal component of its EOF mode in Figs. 2a,b (Figs. 2c,d). The monthly standard deviations of the observed and simulated IOSD and SASD indices are largest in austral summer (Figs. 4a,b), indicating a strong phase locking of their interannual variation to austral summer. This allows us to define IOSD (SASD) events as years when the observed IOSD (SASD) index averaged in austral summer exceeds one standard deviation. This leads to eight positive IOSD (SASD) events: 1960/61, 1965/66, 1967/68, 1973/74, 1975/76, 1980/81, 1981/82, and 1998/99 (1961/62, 1965/66, 1975/76, 1979/80, 1980/81, 1981/82, 1996/97, and 1998/99; see Morioka et al. 2011). In the model simulation for 500 years, we find 75 (74) positive IOSD (SASD) events exceeding one standard deviation for the model. Hereafter, we define year 0 as the year when the subtropical dipole event develops and year 1 the following year.

The evolution of the observed and simulated composite SST anomalies for the positive IOSD is shown in Fig. 5. Both positive and negative SST anomaly poles start to grow from austral spring, reach their peak in austral summer, and decay in austral fall. The pattern correlation between the observed and simulated SST anomalies in the peak phase of December (0)–February (1) is 0.81. A similar evolution of the positive and negative poles associated with the positive SASD is found (Fig. 6). However, the pattern correlation between the observed and simulated SST anomalies in austral summer is relatively low at 0.63. This may be mostly due to
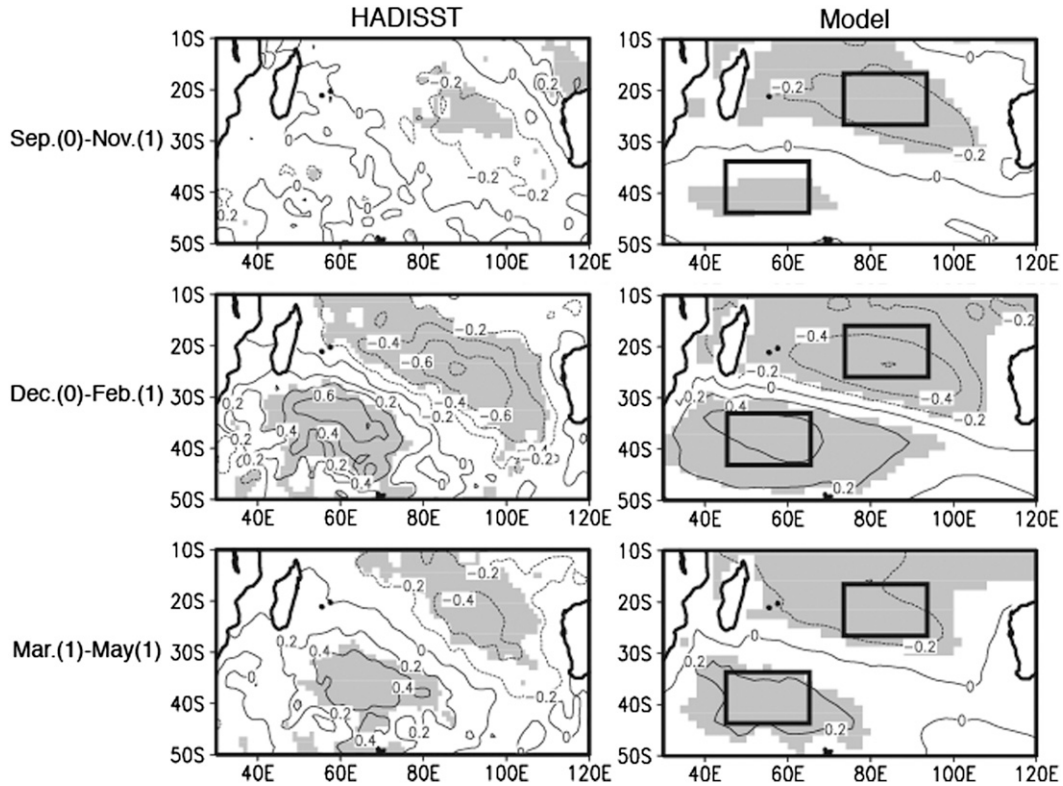
FIG. 5. Evolution of the (left) observed and (right) simulated composite SST anomalies (°C) for the positive IOSD. The boxes over the positive (negative) SST anomaly pole in the right panels are defined as in Fig. 2b. The shading in the left (right) panels indicates anomalies exceeding the 90% (99%) confidence level by a two-tailed t test.

a difference in the position of the positive pole between the observation and model, which is discussed in the final section.

5. Growth and decay mechanisms of the subtropical dipole modes

The model has high skill in reproducing the seasonal and interannual variability in the subtropical region. Because of the lack of observational data, here we use the outputs from the model to explore the mechanism of the subtropical dipole modes. Although the amplitude of the observed SST anomalies during the negative IOSD is slightly different from that during the positive IOSD, the growth and decay mechanisms of the negative IOSD are almost a mirror image of the positive IOSD. Also, the mechanism of the SASD is almost close to that of the IOSD. Therefore, we discuss only the case for the positive IOSD.

a. Growth

Figures 7a and 7b show composite interannual anomalies of each term in Eq. (1) for the positive and negative

SST anomaly poles described in Fig. 5. The mixed layer temperature anomaly over the positive (negative) pole grows from late austral spring to early austral summer owing mostly to the anomalous warming (cooling) from the net surface heat flux. In particular, the anomalous contribution from the shortwave radiation is dominant (Figs. 7c,d). This result supports the results obtained from an OGCM by Morioka et al. (2010, 2011).

1) CONTRIBUTION FROM SHORTWAVE RADIATION

The interannual contribution from the surface heat flux in Eq. (1) is decomposed as

$$\delta\left(\frac{Q_{\text{net}} - q_d}{\rho c_p H}\right)\left[\equiv \delta\left(\frac{Q}{\rho c_p H}\right)\right] = \frac{\delta Q}{\rho c_p \overline{H}} - \frac{\delta H \overline{Q}}{\rho c_p \overline{H}^2} + \text{res} \tag{2}$$

(Morioka et al. 2010, 2011), where an overbar means the monthly climatology, $\delta(\cdots)$ indicates a deviation from the monthly climatology, and $Q = Q_{\text{net}} - q_d$. Each term in Eq. (2) for the shortwave radiation is shown in
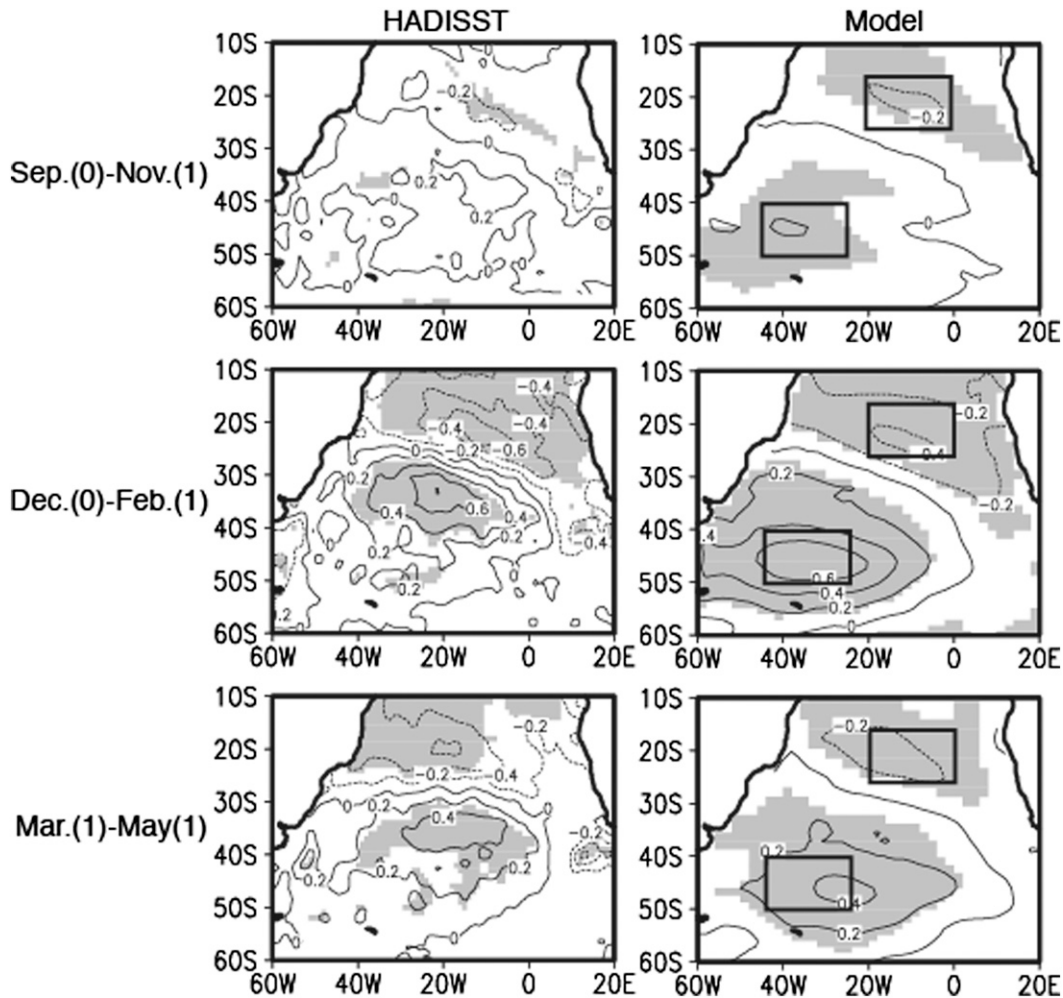
FIG. 6. As in Fig. 5 but for the positive SASD. (right) The boxes over the positive (negative) SST anomaly pole are defined as in Fig. 2d.

Figs. 8a,b. Over the positive (negative) pole the anomalous contribution from the shortwave radiation is due mostly to the second term on the rhs of Eq. (2), indicating that warming of the mixed layer by the climatological shortwave radiation is enhanced (suppressed) by a thinner (thicker) than normal mixed layer, as shown in Fig. 8c (Fig. 8d). On the other hand, cooling of the mixed layer by the climatological latent heat loss in Fig. 9a (Fig. 9b) is enhanced (suppressed) by the same mixed layer thickness anomaly and this cancels out the decreased (increased) latent heat loss in the first term of Eq. (2) as suggested in Fig. 9c (Fig. 9d).

Regarding the oceanic role, the residual term contributes to cooling (warming) the mixed layer anomalously in Fig. 7a (Fig. 7b). Besides the effects of the high frequency variability, this may be related to the fact that the cooling of the mixed layer by detrainment and diffusion is enhanced (reduced) by the thinner (thicker) than normal

mixed layer. On the other hand, the contribution from horizontal advection due to the oceanic circulation is very small. This may be due to the fact that the SST anomaly poles associated with the IOSD are located off the strong Agulhas return current.

The significant role of interannual variations in the mixed layer thickness was overlooked in previous studies by Suzuki et al. (2004) and Hermes and Reason (2005) because they calculated the mixed layer heat balance assuming a constant thickness. This important point was already demonstrated by the OGCM studies (Morioka et al. 2010, 2011).

2) INTERANNUAL VARIABILITY OF THE MIXED LAYER DEPTH

The interannual anomaly in the mixed layer thickness is the key to the evolution of the tendency anomaly in the mixed layer temperature in Eq. (2). This mixed layer
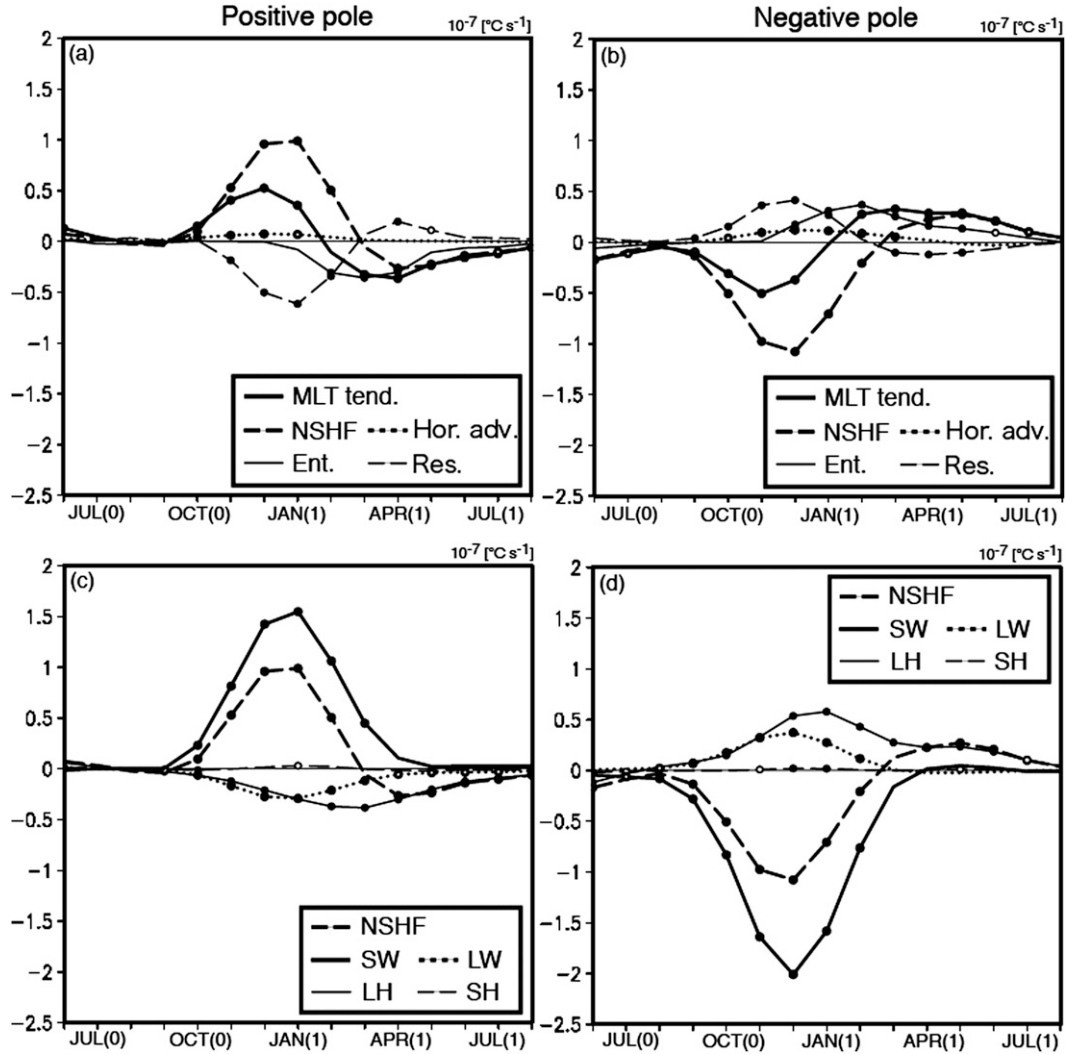
FIG. 7. Time series of composite anomalies of (a),(b) the mixed layer temperature tendency (10^{-7} °C s^{-1}) terms in Eq. (1) and (c),(d) components of the net surface heat flux (10^{-7} °C s^{-1}) terms in Eq. (1) over the positive and negative poles for the positive IOSD. Closed (open) circles show anomalies exceeding the 99% (95%) confidence level by a two-tailed t test. A 3-month running mean is applied to smooth the time series. In the upper panel, the mixed-layer temperature tendency (MLT tend., thick solid line), net surface heat flux (NSHF, thick dashed line), horizontal advection (Hor. adv., thick dotted line), entrainment (Ent., thin solid line) and residual (Res., thin dashed line) terms are shown. In the lower panel, the short wave radiation (SW, thick solid line), long wave radiation (LW, thick dotted line), latent heat flux (LH, thin solid line) and sensible heat flux (SH, thin dashed line) terms are shown.

thickness anomaly may be linked with wind stirring and surface heat flux anomalies. To clarify each contribution quantitatively, we calculate a diagnostic value of the mixed layer depth during a shoaling phase, called the Monin–Obukhov depth:

$$H_{MO} = \left[m_0 u_*^3 + \frac{\alpha g}{\rho c_p} \int_{-H_{MO}}^{0} q(z)\,dz \right] \Big/ \frac{\alpha g}{2\rho c_p} (Q_{net} - q_d)$$

$$(3)$$

(Kraus and Turner 1967; Qiu and Kelly 1993). Here m_0 is a coefficient for the efficiency of wind stirring, and we use $m_0 = 0.5$ (Davis et al. 1981). The frictional velocity u_* is defined by $u_* \equiv (\rho_a C_D u_{10}^2/\rho)^{1/2}$, where ρ_a ($=1.3$ kg m^{-3}) is the density of air, C_D ($=0.00125$) is the drag coefficient, and u_{10} is the wind speed at 10-m height. Also, α ($=0.00025$) is the thermal expansion coefficient, and $q(z)$ is the downward solar insolation (Paulson and Simpson 1977). The interannual anomaly of the
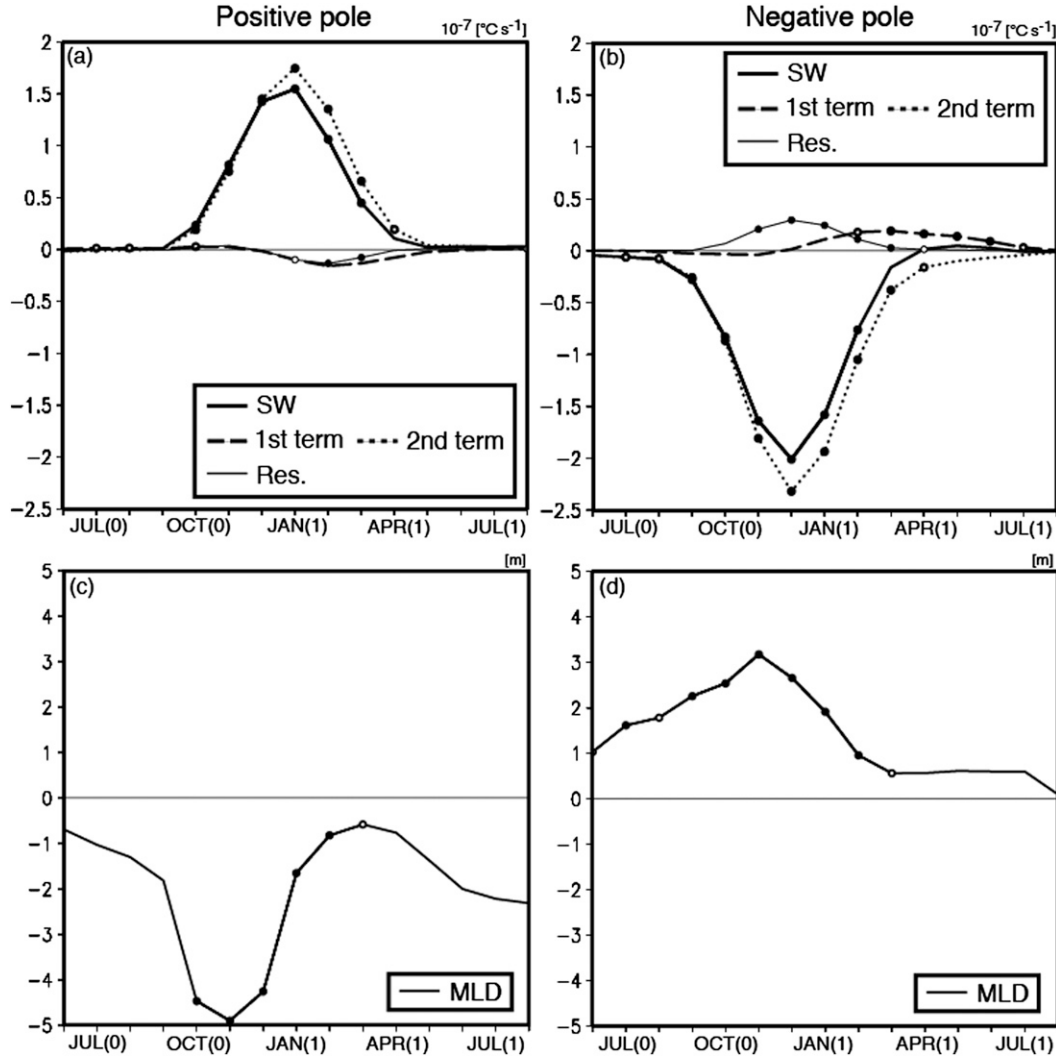
FIG. 8. Time series of composite anomalies of (a),(b) SW (10^{-7} °C s^{-1}) terms in Eq. (2) and (c),(d) mixed layer depth (m), defined as δH in Eq. (2), at the positive and negative poles for the positive IOSD. Closed (open) circles show anomalies exceeding the 99% (95%) confidence level by a two-tailed t test. A 3-month running mean is applied to smooth the time series. In the upper panels, the net SW term (thick solid line; already shown in Figs. 7c,d), first term (thick dashed line), second term (thick dotted line), and Res. term (thin solid line) are shown.

Monin–Obukhov depth and each contribution from the wind stirring and surface heat flux anomalies are calculated by

$$
\delta(H_{\mathrm{MO}})\left[\equiv \delta\left(\frac{m_0 u_*^3 + q_*}{Q_*}\right)\right]
$$
$$
= \frac{m_0 \delta(u_*^3)}{\overline{Q_*}} + \frac{\delta q_*}{\overline{Q_*}} - \frac{\delta Q_*(m_0 \overline{u_*^3} + \overline{q}_*)}{\overline{Q_*}^2} + \mathrm{res}, \quad (4)
$$

where $Q_* = (2\rho c_p)^{-1}\alpha g(Q_{\mathrm{net}} - q_d)$ is the effective buoyancy forcing and $q_* = (\rho c_p)^{-1}\alpha g \int_{-H_{\mathrm{MO}}}^{0} q(z)\,dz$ is

the effective (penetrative) shortwave radiation. Table 1 provides contributions from the wind stirring anomaly (the first term), the surface heat flux anomaly (the second and third terms), and the residual (res) averaged in the growth phase of November (0)–January (1). The interannual anomaly of the Monin–Obukhov depth at each pole explains rather well the mixed layer depth anomaly of December (0) in Figs. 8c,d. This is mostly due to the contribution from the surface heat flux anomaly in which the latent heat flux anomaly plays the major role, as suggested in Figs. 9c,d.
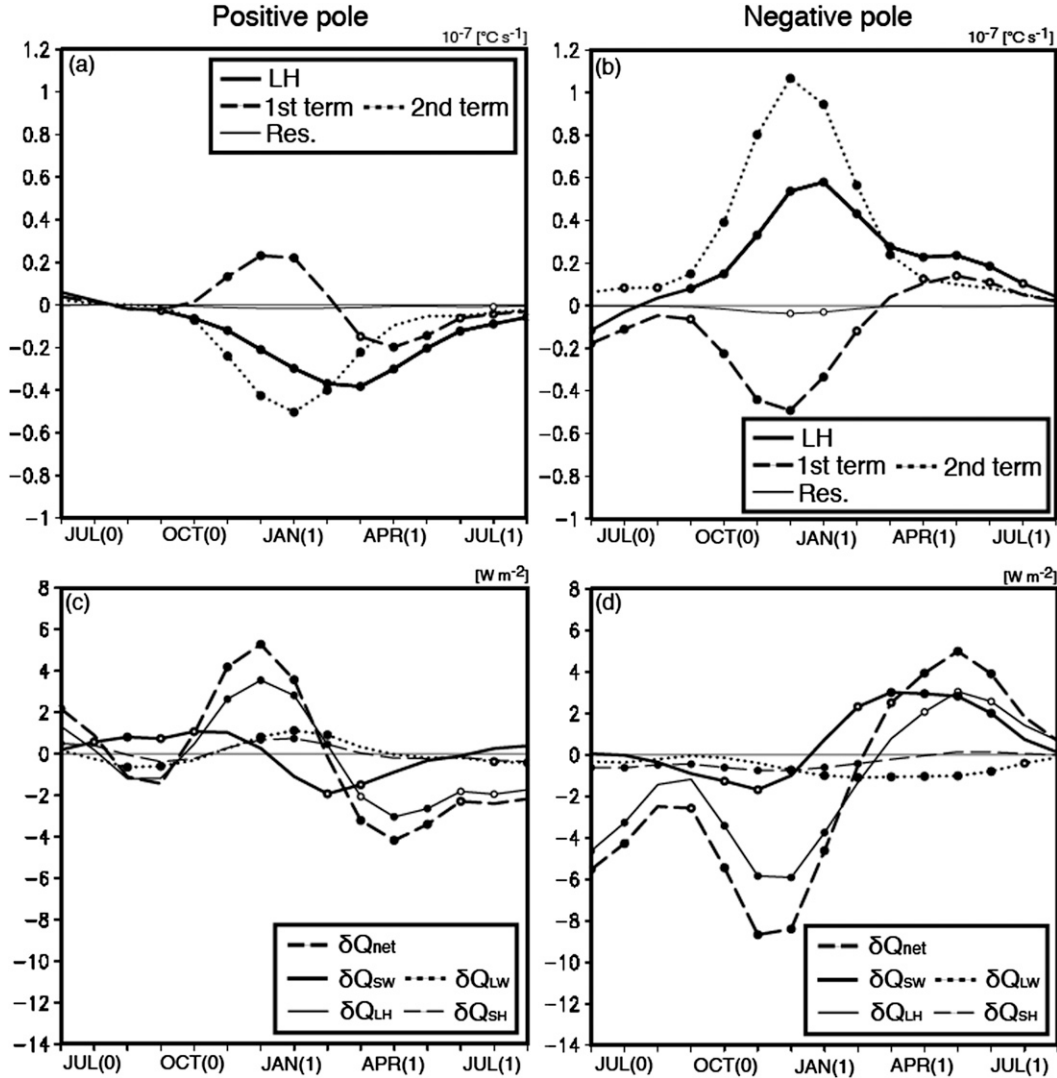
FIG. 9. Time series of composite anomalies of (a),(b) the latent heat flux (10^{-7} °C s^{-1}) terms in Eq. (2) and (c),(d) components of the surface heat flux (W m^{-2}) corresponding to δQ in Eq. (2) over the positive and negative poles for the positive IOSD. Closed (open) circles show anomalies exceeding the 99% (95%) confidence level by a two-tailed t test. A 3-month running mean is applied to smooth the time series. In (a),(b) net LH term (thick solid line; already shown in Figs. 7c,d), first term (thick dashed line), second term (thick dotted line), and residual term (thin solid line) are shown. In (c),(d) δQ_{net}, δQ_{SW}, δQ_{LW}, δQ_{LH}, and δQ_{SH} indicate the NSHF (thick dashed line), SW (thick solid line), LW (thick dotted line), LH (thin solid line), and SH (thin dashed line) anomalies.

3) INTERANNUAL VARIABILITY OF THE LATENT HEAT FLUX

To further investigate the cause of the latent heat flux anomaly in a simple way, we estimate the simulated latent heat flux Q_{LH} using the bulk formula:

$$Q_{\mathrm{LH}} = \rho_a L_E C_E u_{10}(q_s - q_{2\mathrm{m}}), \qquad (5)$$

where L_E is the latent heat of vaporization, C_E is the bulk transfer coefficient of humidity based on the bulk Richardson number, q_s is saturated specific humidity at

the sea surface, and $q_{2\mathrm{m}}$ is specific humidity 2 m above the sea surface. The interannual anomaly of the latent heat flux in Eq. (5) is given by

$$\delta(Q_{\mathrm{LH}}) = \delta(C u_{10} \Delta q) = \delta(C)\overline{u}_{10}\Delta\overline{q} + \delta(u_{10})\overline{C}\Delta\overline{q}$$
$$+ \delta(\Delta q)\overline{C}\overline{u}_{10} + \mathrm{res}, \qquad (6)$$

where $C(=\rho_a L_E C_E)$ is calculated by dividing Q_{LH} by u_{10} $(q_s - q_{2\mathrm{m}})$ in Eq. (5). The latent heat flux anomaly and contribution from each term in Eq. (6) are shown in Fig. 10. Over the positive pole the positive latent heat flux

TABLE 1. Composite anomalies of the Monin–Obukhov depth (m) (MOD), each contribution from the wind stirring (Wind), net surface heat flux (NSHF), and residual (Res) terms in Eq. (4) at the positive and negative SST anomaly poles during November (0)–January (1) of the positive IOSD.

	MOD	Wind	NSHF	Res
Positive pole	−3.2	−0.8	−2.0	−0.4
Negative pole	7.8	1.8	3.8	2.2

anomaly in December (0) is mostly due to both contributions from the bulk transfer coefficient and specific humidity difference anomalies (Fig. 10a). The advection of the anomalous warm air from the tropics associated with both the southward shift and strengthening of the Mascarene high acts to enhance the stability near the ocean surface and decrease the specific humidity difference, leading to the decrease in latent heat loss over the positive pole (Figs. 11a,b). On the other hand, over the negative pole the wind speed anomaly associated with the variation in the Mascarene high is a major contributor to the increase in latent heat flux loss (Fig. 10b). This result is inconsistent with that of Chiodi and Harrison (2007), who suggested the key role of the humidity difference over both poles for one typical positive IOSD in 1997. Since our results apply for the nine positive IOSD events using the NCEP–NCAR reanalysis (figure not shown), we cannot generalize the result by Chiodi and Harrison (2007) over the negative pole. In addition, the latent heat flux and SLP anomalies in Figs. 11a,b are nearly half as large as those in the observation (Behera and Yamagata 2001). This may explain why the amplitude of positive and negative SST anomalies in the model is underestimated (Fig. 5).

b. Decay

After reaching its peak in February (1), the positive (negative) pole decays in early austral fall owing to the anomalous contribution from the entrainment and in late austral fall owing to that from the net surface heat flux, in particular, the latent heat flux, as shown in Figs. 7a,c (Figs. 7b,d).

1) CONTRIBUTION FROM ENTRAINMENT

The anomalous contribution from entrainment can be explained by decomposing the interannual anomaly of the entrainment term in Eq. (1) as

$$-\delta\left(\frac{\Delta T}{H}w_e\right) = -\frac{\delta(\Delta T)\overline{w}_e}{\overline{H}} - \frac{\delta(w_e)\overline{\Delta T}}{\overline{H}} + \frac{\delta H\overline{\Delta Tw_e}}{\overline{H}^2} + \text{res.} \tag{7}$$

(Morioka et al. 2011). In early austral fall this is primarily due to the first term and secondarily to the second

term on the right-hand side (Figs. 12a,b). The contribution from the first term indicates that, over the positive (negative) pole, cooling of the mixed layer by entrainment is enhanced (suppressed) by the positive (negative) anomaly in the temperature difference between the mixed layer and entrained water, which very likely can be attributed to the anomaly in the mixed layer temperature. The contribution from the second term also suggests that the rate of change in mixed layer thickness over the positive (negative) pole anomalously increases (decreases), as suggested in Fig. 8c (Fig. 8d), leading to the increased (decreased) entrainment velocity.

2) CONTRIBUTION FROM LATENT HEAT FLUX

In late austral fall the anomalous contribution from the latent heat flux in Fig. 7c (Fig. 7d) plays a more significant role owing to the anomalous cooling (warming) from the first term in Eq. (2), as shown in Fig. 9a (Fig. 9b). A close examination of Fig. 10a (Fig. 10b) reveals that the latent heat loss increases (decreases) anomalously due to both the increased (decreased) specific humidity difference owing to the warmer (colder) SST and the decreased stability (wind speed) near the surface owing to the weakening of the Mascarene high (figure not shown). Also, the second term in Eq. (2) over the negative pole contributes to its decay in late austral fall (Fig. 9b), indicating that cooling of the mixed layer by the climatological latent heat loss is reduced by the thicker than normal mixed layer (Fig. 8d). The contribution from the second term can be explained as follows. Although the climatological mixed layer depth and the absolute value of its interannual anomaly in late austral fall are not so different between the poles (Figs. 3e,f, 8c,d), the climatological latent heat loss over the negative pole is much larger than that over the positive pole. This larger climatological latent heat loss is mostly due to the stronger wind and larger difference in the specific humidity near the ocean surface on the northeastern flank of the Mascarene high.

6. Impacts of the subtropical dipole modes on the southern African rainfall

A significant part of southern African rainfall occurs in austral summer owing to the southward shift of the south Indian Ocean convergence zone (Cook 2000), where tropical–temperate troughs (Harrison 1984) develop [see Reason et al. (2006) for a review]. This is clearly seen in Fig. 13a, where the northwest–southeast oriented rainfall pattern prevails over southern Africa. In the northwestern (southeastern) part of southern Africa, the westerly (easterly) associated with the Angola low (Mascarene high) helps supply moisture from the South
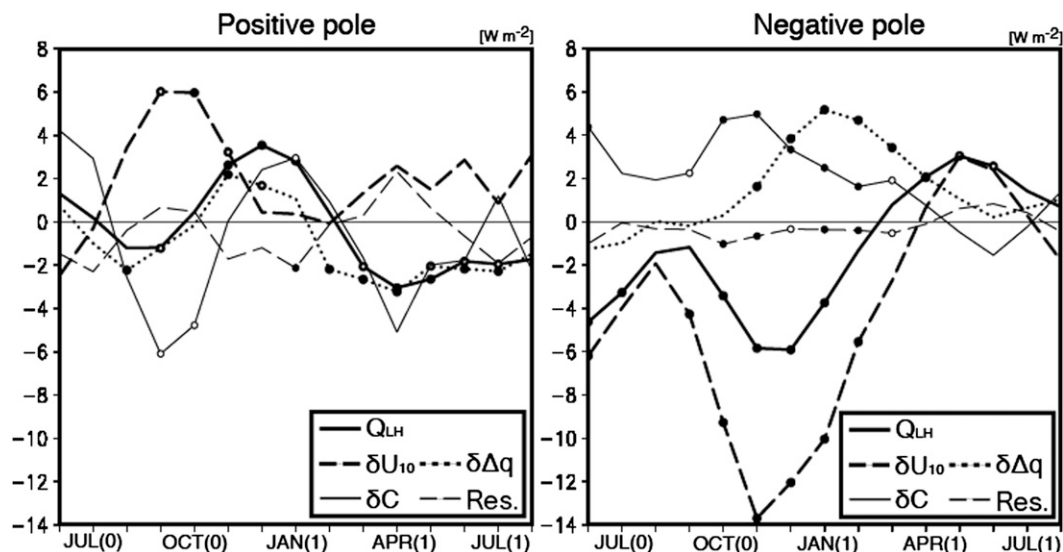
FIG. 10. Time series of composite anomalies of LH (thick solid line; already shown in Figs. 9c,d) and each contribution from the wind speed at 10 m (thick dashed line), specific humidity difference near the surface (thick dotted line), transfer coefficient (thin solid line), and residual (thin dashed line) terms in Eq. (6) over (a) positive and (b) negative poles for the positive IOSD (W m^{-2}). Closed (open) circles show anomalies exceeding the 99% (95%) confidence level by a two-tailed t test. A 3-month running mean is applied to smooth the time series.

Atlantic (southern Indian Ocean). Although the simulated rainfall over Mozambique, South Africa, and Lesotho (Congo basin) is larger (smaller) than observed, the spatial patterns of the low-level wind and associated rainfall over southern Africa are simulated in the model (Fig. 13b).

To study the relative influence of the SASD and IOSD on austral summer rainfall over southern Africa, we classify the years of subtropical dipole modes into three groups: co-occurrence of the SASD and IOSD, pure SASD, and pure IOSD. Here we define years with both SASD and IOSD indices exceeding one (minus one) standard deviation as co-occurring positive (negative) SASD and IOSD events. When only the SASD (IOSD) index exceeds ±1 standard deviation, it is defined as the pure SASD (IOSD) event. This procedure leads to 5 (19) events for the co-occurrence of the positive SASD and

IOSD, 3 (55) pure positive SASDs, and 3 (56) pure positive IOSDs in the observation (model). Similarly, 5 (26) events for the co-occurrence of the negative SASD and IOSD, 6 (47) pure negative SASDs, and 2 (53) pure negative IOSDs in the observation (model) are obtained. Since the number of the observed events for each group is not enough to discuss their composites, we only discuss the positive SASD and IOSD in the model here. We note that the mechanism of the simulated rainfall anomalies for the negative events is close to a mirror of that for the positive events.

The austral summer rainfall slightly increases south of 15°S when the positive SASD and IOSD co-occur (Fig. 14a). In particular, the positive rainfall anomalies near Mozambique and Zambia are statistically significant. To investigate the mechanism of the rainfall anomalies, the anomalous moisture flux and its divergence integrated
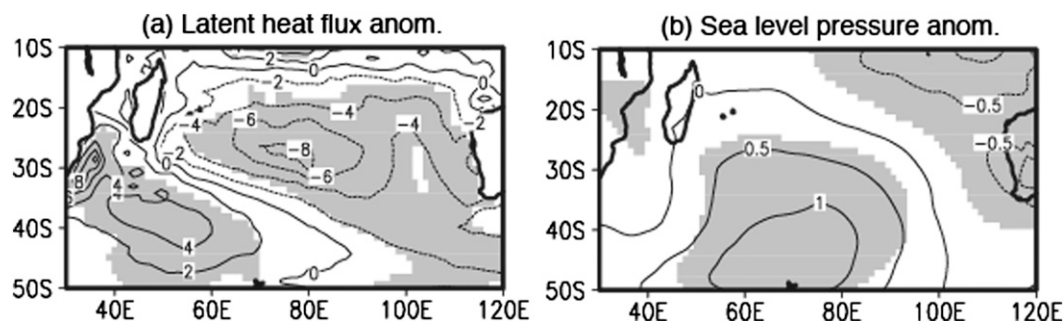

FIG. 11. Composite anomalies of (a) LH (W m^{-2}) and (b) SLP (hPa) averaged during November (0)–January (1) of the positive IOSD. The anomalies exceeding 99% confidence level by two-tailed t test are shaded.
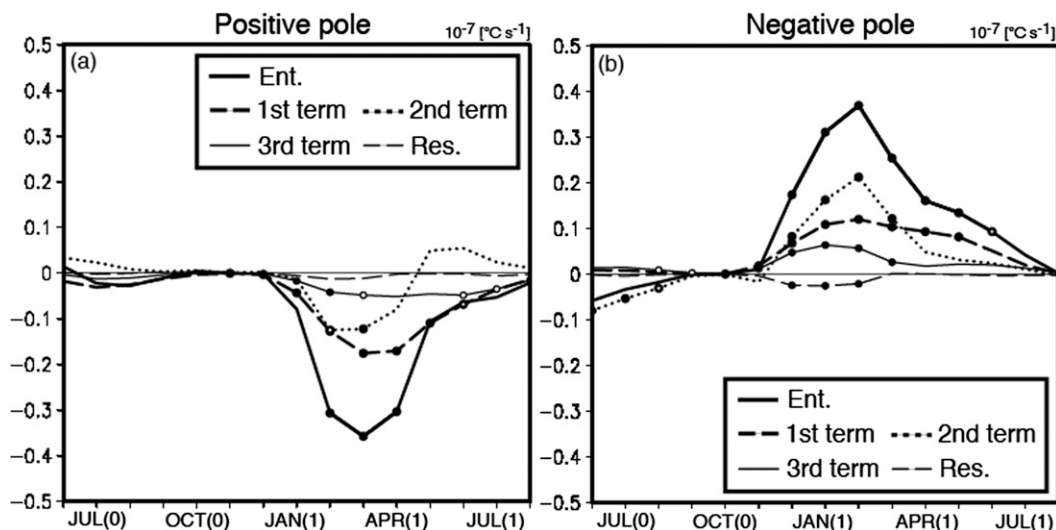
FIG. 12. Time series of composite anomalies of (a),(b) entrainment terms (10^{-7} °C s^{-1}) in Eq. (7) over the positive and negative SST anomaly poles for the positive IOSD. Closed (open) circles show anomalies exceeding the 99% (95%) confidence level by a two-tailed t test. A 3-month running mean is applied to smooth the time series. The net entrainment term (thick solid line; already shown in Figs. 7c,d), first term (thick dashed line), second term (thick dotted line), third term (thin solid line), and residual term (thin dashed line) are shown.

vertically from 300 hPa to the surface are calculated. The moisture flux anomalies for southern Africa south of 10°S rotate cyclonically and converge near Mozambique and Zambia (Fig. 14b). The anomalous moisture advection from the southern Indian Ocean owing to the strengthening of the Mascarene high also contributes to this anomalous convergence, leading to enhanced rainfall. The anomalous increase in rainfall is also found south of 20°S for the pure positive SASD (Fig. 14c). This is mostly due to anomalous moisture advection from the north associated with the anticyclonic circulation anomaly over the Mozambique Channel converging with that from the

south owing to the strengthening of the St. Helena high (Fig. 14d). However, a discrepancy exists between the enhanced rainfall and anomalous divergence of moisture flux over southwestern Africa. Since the monthly outputs of the model are used in the calculation of moisture flux, the high frequency variability, such as migrating disturbances, may be responsible for this difference. For the pure positive IOSD, the rainfall anomalies south of 20°S are not significant (Fig. 14e). Instead, the rainfall near Angola (Madagascar) increases anomalously. This is because the moisture flux anomalies in Fig. 14f rotate cyclonically south of 10°S in southern Africa
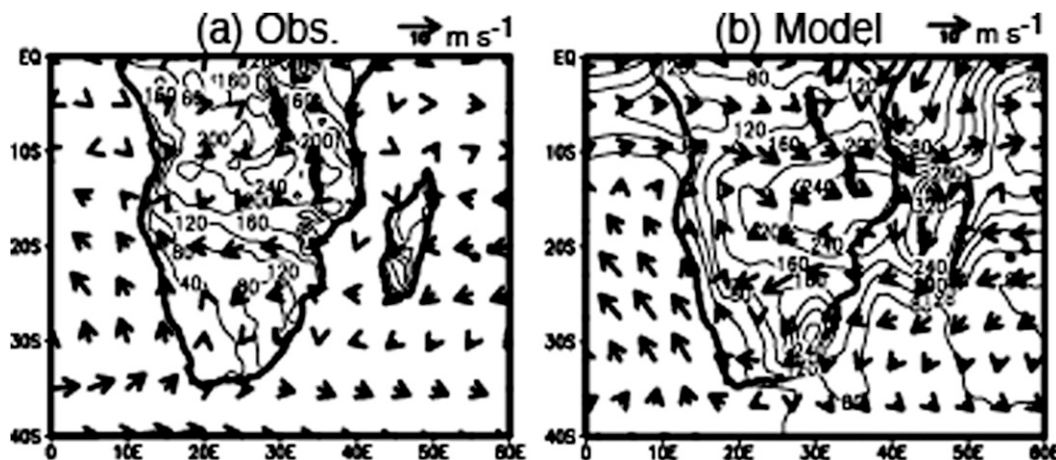

FIG. 13. Austral summer rainfall (contours, mm month^{-1}) and horizontal wind (vectors, m s^{-1}) at 850 hPa in (a) the observations and (b) the model.
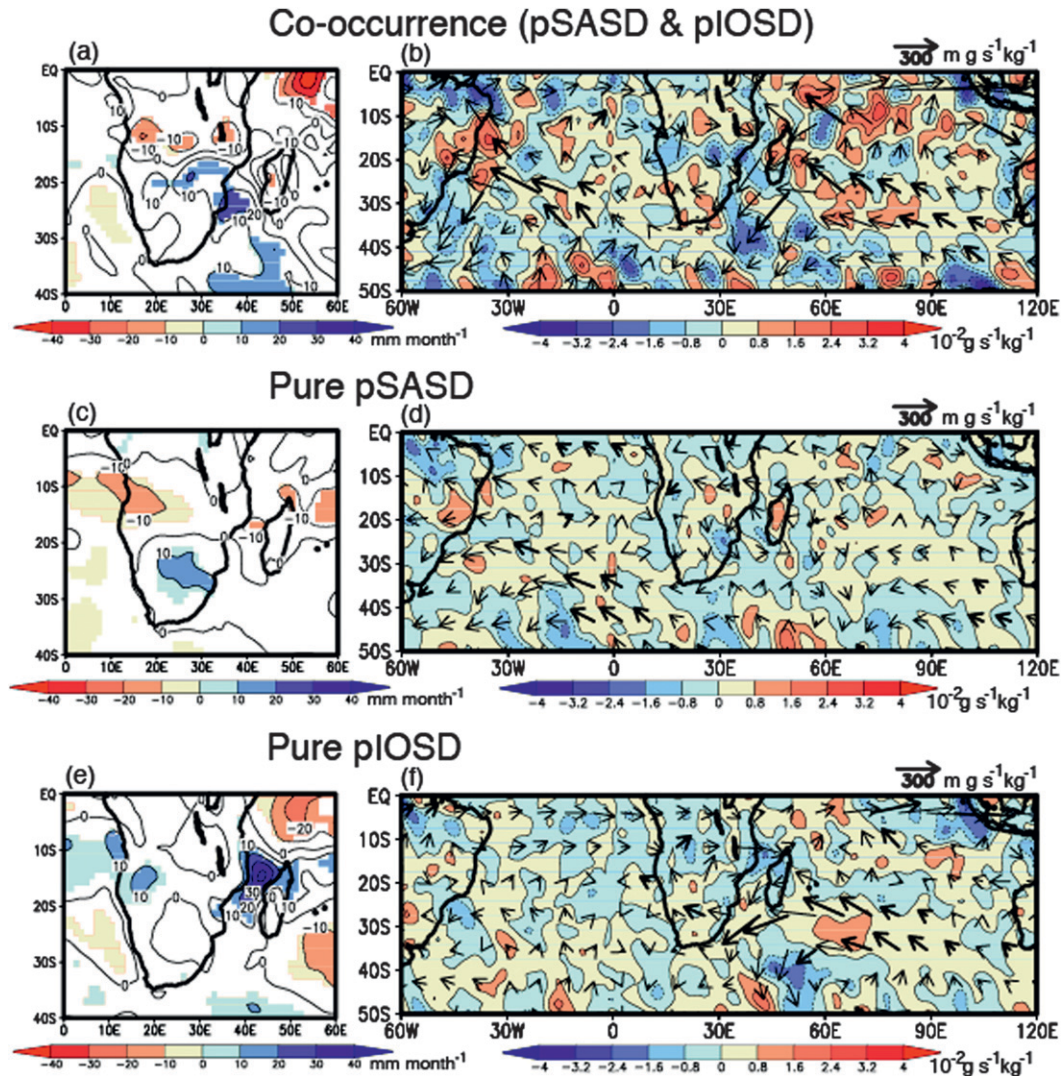
Co-occurrence (pSASD & pIOSD)

Pure pSASD

Pure pIOSD

FIG. 14. Composite anomalies of (a) the simulated southern African rainfall (mm month^{-1}) and (b) moisture flux (arrows, m g s^{-1} kg^{-1}) and its divergence (contours, interval 10^{-2} g s^{-1} kg^{-1}) integrated from 300 hPa to the surface in austral summer for the co-occurrence of the positive SASD and IOSD. As in (a),(b) but (c),(d) for the pure positive SASD and (e),(f) for the pure positive IOSD. The rainfall (moisture flux) anomalies exceeding the 90% confidence level by a two-tailed t test are colored (shown by thick arrows).

and anomalously converge with those from the west (east) in the South Atlantic (southern Indian) Ocean (associated with the strengthening of the Mascarene high). The present result suggests that the pure positive SASD may play a more important role in the enhanced rainfall over the southern part of southern Africa than the pure positive IOSD in our model. This result seems to contrast with the observational result showing an anomalous increase (decrease) in the rainfall over the southern part of southern Africa during the pure positive IOSD (SASD) (figure not shown). However, these rainfall anomalies are not significant because of the limited number of events. Therefore, more observational data is required to verify the relative

importance of the SASD and IOSD for the rainfall variations derived from the model.

7. Conclusions and discussion

Using the outputs from a CGCM, the growth and decay mechanisms of the subtropical dipole modes and their impacts on southern African rainfall are examined. Although the southwestern pole for the simulated SASD is located in higher latitudes, the evolution of the northeastern and southwestern poles for both IOSD and SASD is well reproduced. During the growth phase of the positive event from late austral spring to early austral

summer, the southward migration and strengthening of the subtropical high suppresses (enhances) latent heat flux loss over the southwestern (northeastern) pole through a decrease in the specific humidity difference and increase in the near-surface stability (the increase in the near-surface wind speed). This induces a thinner (thicker) than normal mixed layer, which enhances (suppresses) warming of the mixed layer by climatological shortwave radiation, leading to the generation of the positive (negative) SST anomaly pole. This contradicts previous results by Suzuki et al. (2004) and Hermes and Reason (2005), who suggested the importance of latent heat flux anomalies by calculating the heat balance for a constant mixed layer thickness. Therefore, we have demonstrated that the seasonal and interannual variations in mixed layer thickness play a key role in the growth of the dipoles.

The positive (negative) pole decays in early austral fall mostly because of the anomalous contribution from entrainment and from the latent heat flux in late austral fall. The cooling of the mixed layer by entrainment is enhanced (suppressed) mainly by the larger (smaller) temperature difference between the mixed layer and entrained water owing to the warmer (colder) mixed layer. Also, the warmer (colder) SST acts to enhance (reduce) latent heat loss owing to the larger specific humidity difference near the surface. These CGCM results not only support the OGCM results by Morioka et al. (2010, 2011) but also clarify the cause of the latent heat flux anomalies, which play an important role in generating the mixed layer thickness anomalies during growth of the subtropical dipole modes.

In addition, the coupled model results reveal the significant impact of the subtropical dipole modes on southern African rainfall in austral summer. The rainfall over southern Africa increases anomalously when the positive IOSD and SASD co-occur or when the positive SASD occurs independently of the positive IOSD. This is mostly because of the anomalous convergence of moisture flux linked with the strengthening of the Mascarene high and/or St. Helena high. However, the rainfall anomalies for the pure positive IOSD are not significant in the subtropical region except in Angola and Madagascar. Although further verification using a longer observational database is required, the present coupled model suggests that the positive SASD may have more impact on the rainfall variations over southern Africa than the positive IOSD.

The interannual variations of the Mascarene high and St. Helena high play an important role in rainfall variability over southern Africa as well as in the evolution of the subtropical dipole modes. Although other climate modes such as ENSO also influence rainfall variability, resolving the variability of the subtropical highs may

lead to an improvement of prediction skill for southern African rainfall through better prediction of the subtropical dipole modes. However, the center of SLP anomalies in the South Atlantic associated with the positive SASD is simulated with a southward shift by 10° (Fig. 15). This may be the major cause of model bias in the position of the positive SST anomaly pole for the SASD (Fig. 6). The SLP anomalies in midlatitudes are accompanied by anomalies in the upper troposphere, and those are due to the propagation of stationary Rossby waves. The stationary wavenumber at 200 hPa in austral summer is calculated by $K_S = (\beta_M/U_M)^{1/2}$, where β_M is the effective beta and U_M is the Mercator projection of the basic zonal velocity (Hoskins and Karoly 1981). The maximum stationary wavenumber, which indicates the stationary Rossby waveguide, is simulated for higher latitudes between 50° and 60°S in the South Atlantic (Figs. 15a,b). This is related to the difference of the polar front jet between the reanalysis data and the model (Figs. 15c,d). The amplitude and location of the polar front jet in austral summer are strongly influenced by the SST front through the formation of storm tracks (Nakamura and Shimpo 2004; Sampe et al. 2010). The SST front is clearly located around 45°S in observations, whereas that in the model is broadly located between 40° and 50°S because of its low resolution (Figs. 15e,f). This may make the simulated polar front jet broader and weaker. Also, since the simulated SST in mid high latitudes of the South Atlantic is warmer than observed by 2°C, the stronger meridional temperature gradient due to this warm SST bias may enhance baroclinicity near the surface to accelerate the westerlies in the upper troposphere. This will provide a favorable condition for the southward shift of the polar front jet between 50° and 60°S. Thus, improvement of the SST bias in the model is required for accurate simulation of the variation in the subtropical high.

The major cause of interannual variation in the subtropical high remains unclear. Several studies discussed its possible link with air–sea interaction inside the basin or remote forcings by ENSO, the Indian Ocean dipole, and Antarctic circumpolar waves in midlatitudes (Behera and Yamagata 2001; Fauchereau et al. 2003; Colberg et al. 2004; Hermes and Reason 2005; Terray 2011). However, none of these studies evaluated the relative influence of those climate modes on the variation in the subtropical high. Also, recent studies by Wang (2010a,b) suggested that the subtropical dipole mode exists as a thermodynamical coupled mode, which is linearly independent of ENSO and the southern annular mode. In this regard, further studies using an AGCM and/or CGCM are required to determine the source of the variations in the subtropical high in more detail.
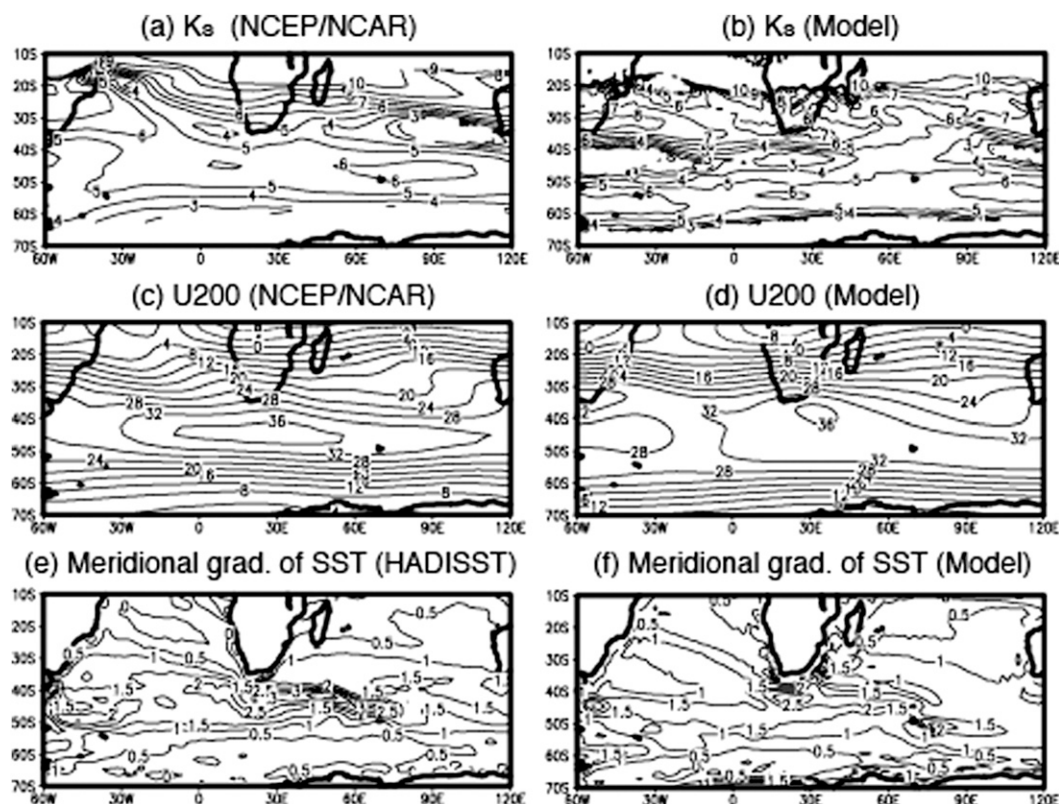
FIG. 15. (a),(b) Stationary wavenumber K_s (in $1/a$ m^{-1}, where a is the earth's radius), (c),(d) zonal wind speed (m s^{-1}) at 200 hPa, and (e),(f) meridional gradient of SST (10^{-5} °C m^{-1}) in austral summer. In the upper and middle panels the stationary wavenumber and zonal wind speed derived from NCEP–NCAR reanalysis and the SINTEX-F model are shown; in the lower panel the meridional gradient of SST from (e) HADISST and (f) the model is shown.

REFERENCES

Behera, S. K., and T. Yamagata, 2001: Subtropical SST dipole events in the southern Indian Ocean. *Geophys. Res. Lett.,* **28,** 327–330.

——, P. S. Salvekar, and T. Yamagata, 2000: Simulation of interannual SST variability in the tropical Indian Ocean. *J. Climate,* **13,** 3487–3499.

Blanke, B., and P. Delecluse, 1993: Variability of the tropical Atlantic Ocean simulated by a general circulation model with two different mixed-layer physics. *J. Phys. Oceanogr.,* **23,** 1363–1388.

Chiodi, A. M., and D. E. Harrison, 2007: Mechanisms of summertime subtropical southern Indian Ocean sea surface temperature variability: On the importance of humidity anomalies and the meridional advection of water vapor. *J. Climate,* **20,** 4835–4852.

Colberg, F., and C. J. C. Reason, 2007: Ocean model diagnosis of low-frequency climate variability in the South Atlantic region. *J. Climate,* **20,** 1016–1034.

——, ——, and K. Rodgers, 2004: South Atlantic response to El Niño-Southern Oscillation induced climate variability in an ocean general circulation model. *J. Geophys. Res.,* **109,** C12015, doi:10.1029/2004JC002301.

Cook, K. H., 2000: The South Indian Ocean convergence zone and interannual rainfall variability over southern Africa. *J. Climate,* **13,** 3789–3804.

Davis, R. E., R. de Szoeke, and P. Niiler, 1981: Variability in the upper ocean during MILE. Part II: Modeling the mixed layer response. *Deep-Sea Res.,* **28,** 1453–1475.

Fauchereau, N., S. Trzaska, Y. Richard, P. Roucou, and P. Camberlin, 2003: Sea-surface temperature co-variability in the southern Atlantic and Indian Oceans and its connections with the atmospheric circulation in the Southern Hemisphere. *Int. J. Climatol.,* **23,** 663–677, doi:10.1002/joc.905.

——, B. Pohl, C. J. C. Reason, M. Rouault, and Y. Richard, 2009: Recurrent daily OLR patterns in the Southern Africa/Southwest Indian Ocean region, implications for South African rainfall and teleconnections. *Climate Dyn.,* **32,** 575–591.

Gent, P. R., and J. C. McWilliams, 1990: Isopycnal mixing in ocean circulation models. *J. Phys. Oceanogr.,* **20,** 150–155.

Gualdi, S., A. Navarra, E. Guilyardi, and P. Delecluse, 2003: Assessment of the tropical Indo-Pacific climate in the SINTEX CGCM. *Ann. Geophys.,* **46,** 1–26.

Guilyardi, E., P. Delecluse, S. Gualdi, and A. Navarra, 2003: Mechanisms for ENSO phase change in a coupled GCM. *J. Climate,* **16,** 1141–1158.

Harrison, M. S. J., 1984: A generalized classification of South African summer rain-bearing synoptic systems. *J. Climatol.,* **4,** 547–560.

Hermes, J. C., and C. J. C. Reason, 2005: Ocean model diagnosis of interannual coevolving SST variability in the South Indian and South Atlantic Oceans. *J. Climate,* **18,** 2864–2882.

Hoskins, B. J., and D. J. Karoly, 1981: The steady linear response of a spherical atmosphere to thermal and orographic forcing. *J. Atmos. Sci.,* **38,** 1179–1196.

Kalnay, E., and Coauthors, 1996: The NCEP/NCAR 40-Year Reanalysis Project. *Bull. Amer. Meteor. Soc.,* **77,** 437–471.

Kataoka, T., T. Tozuka, Y. Masumoto, and T. Yamagata, 2012: The Indian Ocean subtropical dipole mode simulated in the CMIP3 models. *Climate Dyn.,* doi:10.1007/s00382-011-1271-2, in press.

Kraus, E. B., and J. S. Turner, 1967: A one-dimensional model of the seasonal thermocline: II. The general theory and its consequences. *Tellus,* **19,** 98–106.

Legates, D. R., and C. J. Willmott, 1990: Mean seasonal and spatial variability in gauge-corrected, global precipitation. *Int. J. Climatol.,* **10,** 111–127.

Lindesay, J. A., 1988: Southern African rainfall, the Southern Oscillation and a Southern Hemisphere semi-annual cycle. *J. Climatol.,* **8,** 17–30.

Locarnini, R. A., A. V. Mishonov, J. I. Antonov, T. P. Boyer, H. E. Garcia, O. K. Baranova, M. M. Zweng, and D. R. Johnson, 2010: *Temperature.* Vol. 1, *World Ocean Atlas 2009,* NOAA Atlas NESDIS 68, 184 pp.

Louis, J. F., 1979: A parametric model of vertical eddy fluxes in the atmosphere. *Bound.-Layer Meteor.,* **17,** 187–202.

Luo, J. J., S. Masson, S. Behera, P. Delecluse, S. Gualdi, A. Navarra, and T. Yamagata, 2003: South Pacific origin of the decadal ENSO-like variation as simulated by a coupled GCM. *Geophys. Res. Lett.,* **30,** 2250, doi:10.1029/2003GL018649.

——, ——, E. Roeckner, G. Madec, and T. Yamagata, 2005: Reducing climatology bias in an ocean–atmosphere CGCM with improved coupling physics. *J. Climate,* **18,** 2344–2360.

Madec, G., P. Delecluse, M. Imbard, and C. Levy, 1998: OPA 8.1 ocean general circulation model reference manual. Tech. Note 11, LODYC/IPSL, 91 pp.

Mason, S. J., 1995: Sea-surface temperature—South African rainfall associations, 1910-1989. *Int. J. Climatol.,* **15,** 119–135.

Moisan, J. R., and P. P. Niiler, 1998: The seasonal heat budget of the North Pacific: Net heat flux and heat storage rates (1950–1990). *J. Phys. Oceanogr.,* **28,** 401–421.

Morioka, Y., T. Tozuka, and T. Yamagata, 2010: Climate variability in the southern Indian Ocean as revealed by self-organizing maps. *Climate Dyn.,* **35,** 1059–1072.

——, ——, and ——, 2011: On the growth and decay of the subtropical dipole mode in the South Atlantic. *J. Climate,* **24,** 5538–5554.

Nakamura, H., and A. Shimpo, 2004: Seasonal variations in the Southern Hemisphere storm tracks and jet streams as revealed in a reanalysis dataset. *J. Climate,* **17,** 1828–1844.

North, G. R., T. L. Bell, R. F. Cahalan, and F. J. Moeng, 1982: Sampling errors in the estimation of empirical orthogonal functions. *Mon. Wea. Rev.,* **110,** 699–706.

Paulson, C. A., and J. J. Simpson, 1977: Irradiance measurements in the upper ocean. *J. Phys. Oceanogr.,* **7,** 952–956.

Qiu, B., and K. A. Kelly, 1993: Upper-ocean heat balance in the Kuroshio Extension region. *J. Phys. Oceanogr.,* **23,** 2027–2041.

Rayner, N. A., D. E. Parker, E. B. Horton, C. K. Folland, L. V. Alexander, D. P. Rowell, E. C. Kent, and A. Kaplan, 2003: Global analyses of sea surface temperature, sea ice, and night marine air temperature since the late nineteenth century. *J. Geophys. Res.,* **108,** 4407, doi:10.1029/2002JD002670.

Reason, C. J. C., 1998: Warm and cold events in the southeast Atlantic/southwest Indian Ocean region and potential impacts on circulation and rainfall over southern Africa. *Meteor. Atmos. Phys.,* **69,** 49–65.

——, 2001: Subtropical Indian Ocean SST dipole events and southern African rainfall. *Geophys. Res. Lett.,* **28,** 2225–2227.

——, 2002: Sensitivity of the southern African circulation to dipole sea-surface temperature patterns in the South Indian Ocean. *Int. J. Climatol.,* **22,** 377–393, doi:10.1002/joc.744.

——, and H. Mulenga, 1999: Relationships between South African rainfall and SST anomalies in the southwest Indian Ocean. *Int. J. Climatol.,* **19,** 1651–1673.

——, R. J. Allan, J. A. Lindesay, and T. J. Ansell, 2000: ENSO and climatic signals across the Indian Ocean basin in the global context: Part I, interannual composite patterns. *Int. J. Climatol.,* **20,** 1285–1327.

——, W. Landman, and W. Tennant, 2006: Seasonal to decadal prediction of southern African climate and its links with variability of the Atlantic Ocean. *Bull. Amer. Meteor. Soc.,* **87,** 941–955.

Richard, Y., S. Trzaska, P. Roucou, and M. Rouault, 2000: Modification of the southern African rainfall variability/ENSO relationship since the late 1960s. *Climate Dyn.,* **16,** 883–895.

Roeckner, E., and Coauthors, 1996: The atmospheric general circulation model ECHAM-4: Model description and simulation of present-day climate. Max-Planck-Institut für Meteorologie Rep. 218, 90 pp.

Ropelewski, C., and M. S. Halpert, 1987: Global and regional scale precipitation patterns associated with the El Niño/Southern Oscillation. *Mon. Wea. Rev.,* **115,** 1606–1626.

Sampe, T., H. Nakamura, A. Goto, and W. Ohfuchi, 2010: Significance of a midlatitude SST frontal zone in the formation of a storm track and an eddy-driven westerly jet. *J. Climate,* **23,** 1793–1814.

Sterl, A., and W. Hazeleger, 2003: Coupled variability and air-sea interaction in the South Atlantic Ocean. *Climate Dyn.,* **21,** 559–571.

Suzuki, R., S. K. Behera, S. Iizuka, and T. Yamagata, 2004: Indian Ocean subtropical dipole simulated using a coupled general circulation model. *J. Geophys. Res.,* **109,** C09001, doi:10.1029/2003JC001974.

Terray, P., 2011: Southern Hemisphere extra-tropical forcing: A new paradigm for El Niño-Southern Oscillation. *Climate Dyn.,* **36,** 2171–2199.

Tiedtke, M., 1989: A comprehensive mass flux scheme for cumulus parameterization in large-scale models. *Mon. Wea. Rev.,* **117,** 1779–1800.

Valcke, S., L. Terray, and A. Piacentini, 2000: The OASIS coupler user's guide version 2.4. Tech. Rep. TR/CMGC/00-10, CER-FACS, 85 pp.

Venegas, S. A., L. A. Mysak, and D. N. Straub, 1997: Atmosphere–ocean coupled variability in the South Atlantic. *J. Climate,* **10,** 2904–2920.

Vigaud, N., Y. Richard, M. Rouault, and N. Fauchereau, 2009: Moisture transport between the South Atlantic Ocean and southern Africa: Relationships with summer rainfall and associated dynamics. *Climate Dyn.,* **32,** 113–123.

Walker, N. D., 1990: Links between South African summer rainfall and temperature variability of the Agulhas and Benguela current systems. *J. Geophys. Res.,* **95,** 3297–3319.

Wang, F., 2010a: Thermodynamic coupled modes in the tropical atmosphere–ocean: An analytical solution. *J. Atmos. Sci.,* **67,** 1667–1677.

——, 2010b: Subtropical dipole mode in the Southern Hemisphere: A global view. *Geophys. Res. Lett.,* **37,** L10702, doi:10.1029/2010GL042750.

Yasuda, I., T. Tozuka, M. Noto, and S. Kouketsu, 2000: Heat balance and regime shifts of the mixed layer in the Kuroshio Extension. *Prog. Oceanogr.,* **47,** 257–278.